CONDENSED MATTER PHYSICS

Internal strain tunes electronic correlations on the nanoscale

A. Pustogow[1]*†, A. S. McLeod[2,3]*†, Y. Saito[1,4], D. N. Basov[2,3], M. Dressel[1]*

In conventional metals, charge carriers basically move freely. In correlated electron materials, however, the electrons may become localized because of strong Coulomb interactions, resulting in an insulating state. Despite considerable progress in the last decades, elucidating the driving mechanisms that suppress metallic charge transport, the spatial evolution of this phase transition remains poorly understood on a microscopic scale. Here, we use cryogenic scanning near-field optical microscopy to study the metal-to-insulator transition in an electronically driven charge-ordered system with a 20-nm spatial resolution. In contrast to common mean-field considerations, we observe pronounced phase segregation with a sharp boundary between metallic and insulating regions evidencing its first-order nature. Considerable strain in the crystal spatially modulates the effective electronic correlations within a few micrometers, leading to an extended "zebra" pattern of metallic and insulating stripes. We can directly monitor the spatial strain distribution via a gradual enhancement of the optical conductivity as the energy gap is depressed. Our observations shed new light on previous analyses of correlation-driven metal-insulator transitions.

INTRODUCTION

Phase transitions in condensed matter manifest themselves as distinct changes of physical quantities, such as structure, magnetization, or electrical resistivity, when a tuning parameter is varied (e.g., external pressure, electric or magnetic field, or temperature). Starting from theoretical considerations of the free energy, Landau provided an appropriate description of phase transitions in mean-field approximation (1), which predicts a smooth second-order transition for electronic charge order (CO) or antiferromagnetism, for instance, while the discontinuous variation of the order parameter at a structural and symmetry change defines a first-order phase transition. For numerous strongly correlated electron systems, the situation does not appear that simple and a clear-cut distinction is difficult because several physical interactions become simultaneously important and the dominant states are not spatially homogeneous (2–5). Among the family of transition metal oxides, the complex Verwey transition in magnetite Fe_3O_4 was already found 80 years ago; more recently, manganites exhibiting colossal magnetoresistance have been the subject of intense studies (2, 6). The challenge has been to explain the favorability and mechanisms of intrinsic phase coexistence, which, in the case of first-order transitions, is usually simply a metastable configuration and not otherwise intrinsic (6). Disorder, strain, and long-range magnetic and Coulomb interactions have been proposed as key agents responsible for phase coexistence in these materials, and the relative impact of these phenomena remains debated. Similarly, the geometric morphology of insulator-metal coexistence in vanadate thin films has been attributed to long-range strain interactions amid a coupled structural phase transition (4, 5, 7), whereas local disorder-mediated physics has been found to dominate in some VO_2 and nickelate films (7–9). Overall, the spatial character of phase coexistence predominant in these systems can reveal both the energetics and microscopic physics that control their phase transitions. It is, thus, imperative to investigate the phenomenon and the novel phases emerging from spatial complexity (9), with the appropriate spatial resolution in the submicrometer range.

Beside transition metal oxides, molecular conductors with quarter-filled bands are the prime examples for charge localization driven by long-range Coulomb interactions (10). In quasi one-dimensional Fabre salts, for instance, the molecular charge is periodically modulated in a 0101 pattern and the charge disproportionation 2δ grows in a mean-field fashion below the transition temperature T_{CO} (11, 12). For higher-dimensional systems, however, a more abrupt jump of 2δ was reported, e.g., in layered BEDT-TTF [(bis-(ethylenedithio)tetrathiafulvalene)] salts (13–15) and many inorganic materials (16) exhibiting a charge-disproportionate insulating state. As 2δ is considered the order parameter of the CO transition, the nature of the electronically driven phase transition seems to be not of second order, in contrast to common notion. The subtle involvement of the lattice, as well as the existence of ordered regions separated by domain walls, may be decisive (17, 18).

In this regard, the molecular conductor α-(BEDT-TTF)$_2$I$_3$ is particularly intriguing because the metal-insulator transition is exceptionally abrupt, but structural modifications are minor (17, 19). Although electronic charge ordering in this material is seemingly at odds with a second-order scenario, no distinct evidence of phase segregation with a phase boundary separating the metallic and insulating regions was reported so far, despite several attempts to spatially map the transition (20, 21). The recent advances in nanoscopic measurement techniques open up a completely new view that was not possible before (4, 5, 22). Here, we want to address the question how the metal-insulator phase transition of an electronically correlated solid proceeds on the nanometer scale and eventually resolve the controversially discussed nature of the phase transition.

The problem can only be tackled via a local probe that allows spatially resolved measurements of a physical quantity subject to pronounced changes upon the phase transition. Despite its natural strength in microscopically identifying metallic and insulating states, as demonstrated for the Mott transition in κ-(BEDT-TTF)$_2$X (23, 24), optical spectroscopy is limited by diffraction to length scales of tens of micrometers in the relevant infrared range. On the other hand, common atomic force microscopy (AFM) is not suitable for study of metal-insulator transitions, as it is

[1]1. Physikalisches Institut, Universität Stuttgart, 70569 Stuttgart, Germany. [2]University of California San Diego, La Jolla, CA 92093, U.S.A. [3]Department of Physics, Columbia University, New York, NY 92093, U.S.A. [4]Department of Physics, Hokkaido University, Sapporo 060-0810, Japan.
*Corresponding author. Email: andrej.pustogow@pi1.physik.uni-stuttgart.de (A.P.); dressel@pi1.physik.uni-stuttgart.de (M.D.); am4734@columbia.edu (A.S.M.)
†These authors contributed equally to this work.

insensitive to the electronic properties of the material; conductive AFM is meanwhile insensitive to the local conductivity without a continuous conductive path to the region under study. Scanning tunneling microscopy (STM) is in principle very powerful for this kind of problem; however, tunneling methods face severe difficulties with insulators, and the extreme surface sensitivity makes them inapplicable for many materials. The method of choice is therefore cryogenic scanning near-field optical microscopy (cryo-SNOM), which combines the advantages of optical spectroscopy and scanning probe techniques, and has recently been extended to operate at temperatures suitably low to study the electronic ground state of many canonical correlated electron systems (5). Upon illumination by tightly focused infrared radiation at the metallic tip apex of an AFM probe, an electric field builds up between the tip and the locally induced "image" charges at the nearby sample surface (3, 25). The resultant electric near-field interaction between the probe and the sample modulates the amplitude of radiation scattered into the far-field, which is detected as a sensitive measure of the sample's 20-nm–resolved local dielectric response (compare the sketch in Fig. 1F and Methods). The effective probing depth of the near field into the material is of order of tens of nanometers (26), containing more than 10^3 unit cells. Thus, complications associated with chemical and/or structural modifications of the topmost layers beneath the sample surface do not significantly affect; in other words, we effectively probe the bulk material. The lateral resolution is limited by the AFM tip apex geometry (~10 to 20 nm), which is orders of magnitude below the diffraction limit of the probed wavelengths (3, 25) that confines optical far-field investigations (23, 24).

In our low-temperature optical near-field experiments, we succeeded in tracing the metal-insulator transition in a bulk single-crystalline material with strong electronic correlations. While previous near-field studies on correlated compounds were confined to room temperature and slightly above (8, 27), cryogenic mapping of thin films could be achieved only very recently (5, 9). Here, we expand the realm of applications for this technique by investigating low-temperature phase transitions in the most commonly studied type of materials—bulk single crystals—in condensed matter research. In particular, we record the spatial phase segregation between metallic and insulating regions, as the molecular conductor α-(BEDT-TTF)$_2$I$_3$ is cooled through the metal-insulator transition at T_{CO} = 136 K associated with electronically driven CO (14, 17). By probing the opening of the optical gap in the insulating state, we identify charge-ordered and metallic regions separated by a sharp phase boundary; our findings thus truly prove the first-order nature of the transition. Furthermore, we expose a specimen to tensile stress via mounting on a substrate with a different thermal expansion, causing the crystal to crack; by analyzing the complex phase arrangement emanating from internal strain, we find a local suppression of CO by more than 6 K, which corresponds to an equivalent hydrostatic pressure of 0.6 to 0.7 kbar. Our results demonstrate possible difficulties in assigning phase transitions on the basis of macroscopic measurements, or even the risk of misinterpretation, resulting from improper mounting or a lack of homogeneous samples.

RESULTS

Material properties

For our experiments, we have chosen the charge-transfer salt α-(BEDT-TTF)$_2$I$_3$ that consists of alternating layers of BEDT-TTF$^{+0.5}$ radical cations and I$_3^-$ anions (Fig. 1A). The quasi–two-dimensional compound has a three-fourth–filled conduction band with rather good metallic properties within the plane under ambient conditions.
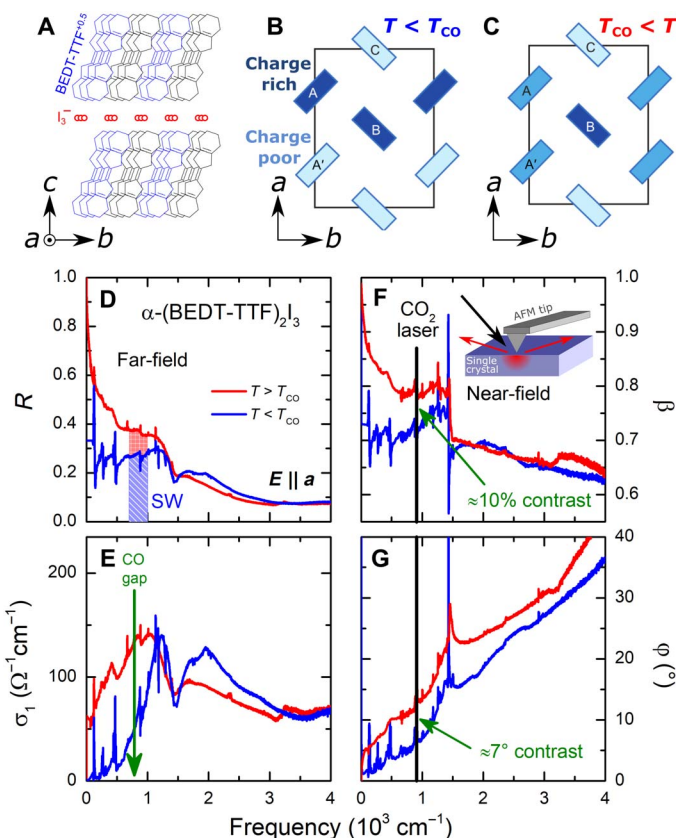

Fig. 1. Electronic properties of α-(BEDT-TTF)$_2$I$_3$ with a metal-insulator transition at T_{CO} = 136 K. (**A**) The crystal structure contains layers of BEDT-TTF molecules slightly tilted along the ab plane, which are separated by sheets of I$_3^-$ anions. (**B**) A significant charge disproportionation develops below the CO transition ($T < T_{CO}$), with charge-rich (A and B) and charge-poor (A' and C) molecules alternating along the a direction, forming a stripe-like pattern oriented parallel to b (28). (**C**) In the normal state ($T_{CO} < T$), the charges of the four inequivalent lattice sites are close to the average value 0.5 e. (**D**) The far-field reflectivity R exhibits pronounced changes upon crossing the CO transition (17). Integrating R in the shaded region (700 to 1000 cm^{-1}) yields distinct values above (T = 150 K, red) and below (T = 120 K, blue) T_{CO}. (**E**) The drop in the optical conductivity below 1000 cm^{-1} indicates the opening of a gap in the density of states when CO sets in. (**F**) The near-field amplitude β and (**G**) the corresponding phase change φ are calculated according to Eq. 1. Both quantities exhibit distinct variations at the CO$_2$ laser frequency of 910 cm^{-1}. The illustration in (F) sketches the electromagnetic near-field (red) arising from interaction of the crystal with the AFM tip upon illumination with the laser radiation (black arrow), reaching well below the sample surface. β corresponds to the scattered light detected in the experiment (red arrows). Figure reproduced from (55).

Strong intersite Coulomb repulsion V leads to a redistribution of charge δ between the organic molecules below T_{CO} = 136 K, as indicated in Fig. 1 (B and C). At the phase transition, the dc conductivity drops by several orders of magnitude and the charge disproportionation 2δ sets in rapidly within a fraction of a kelvin as well (17). Upon applying hydrostatic pressure to α-(BEDT-TTF)$_2$I$_3$, the bandwidth W increases and the effective electronic correlations V/W are reduced. As a consequence, the charge-ordered state is suppressed with an initial rate of 8 K/kbar (28). Note that, eventually, massless Dirac electrons are observed in its high-pressure phase at low temperatures (29, 30).

It can be seen from Fig. 1 (D to G) that the low-frequency optical properties are strongly affected by the CO transition. When the metallic
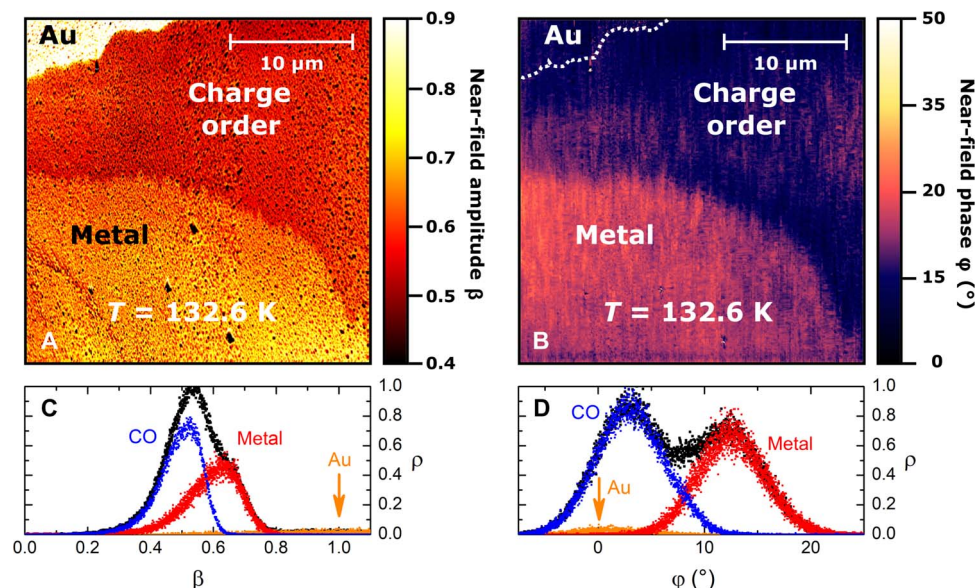
Fig. 2. Near-field image at the boundary between the metallic and charge-ordered regions in α-(BEDT-TTF)₂I₃. (**A**) The near-field amplitude β measured with a CO₂ laser at $T = 132.6$ K slightly below T_{CO}. The metallic regions give a larger amplitude than the CO phase. The bright area in the top left corner stems from the evaporated gold (thickness, 30 nm) used as reference. (**B**) In addition, the phase φ shows considerable contrast between the metallic and insulating regions. The position of the phase boundaries in (A) and (B) match perfectly. (**C**) An intensity histogram of the metallic (red) and charge-ordered (blue) regions normalized to the signal of the gold (Au) layer. (**D**) The respective maxima of the phase histogram are separated by an angle of ≈10°. Figure reproduced from (55).

crystal turns insulating at T_{CO}, the Drude weight vanishes because of the opening of an optical gap (17), leading to a pronounced drop of both the reflectivity and conductivity at frequencies below approximately 1000 cm⁻¹ (Fig. 1, D and E). Intuitively, similar changes are expected for the near-field response. Whereas Fig. 1D displays the far-field optical reflectivity across the CO transition, the optical behavior of the sample under local illumination by quasi-static fields from the near-field probe is described differently. The relevant reflection amplitude β and the phase φ are well approximated from the complex reflection coefficient $r = r_1 + ir_2$ as (31)

$$r = \frac{\varepsilon - 1}{\varepsilon + 1}, \quad \beta = |r|, \quad \varphi = \arctan \frac{r_2}{r_1} \text{ with } \varepsilon = \sqrt{\varepsilon_\parallel \varepsilon_\perp} \quad (1)$$

where $\varepsilon_\parallel$ and $\varepsilon_\perp$ denote the complex dielectric function $\varepsilon = \varepsilon_1 + i\varepsilon_2$ parallel and perpendicular to the surface, respectively. For the investigated crystals, the highly conducting ab plane is parallel to the sample surface, while the c axis points perpendicular (compare the sketch of crystal structure in Fig. 1A). The small anisotropy within the conducting plane is accounted for by averaging between the two in-plane directions $\varepsilon_\parallel = \frac{1}{2}(\varepsilon_a + \varepsilon_b)$. As the overall temperature dependence is similar (17), we display only the a-polarization in Fig. 1 (D and E). Since moderate optical contrasts observed by near-field microscopy associate (to first order) with contrasts in optical reflectivity (31), we regard our measurements as a relative local probe of β. We therefore expect the amplitude of the sample's near-field response to show considerable modifications upon the CO metal-insulator transition, becoming more pronounced toward frequencies lower than the gap energy (<1000 cm⁻¹). As shown in Fig. 1F, the contrast in the amplitude of β is approximately 10% at the CO₂ laser wavelength $\lambda_L = 11$ μm (910 cm⁻¹) used in our near-field experiments. Moreover, given that our implementation of near-field microscopy is sensitive also to the phase of the optical response (Methods), the relevant phase difference δφ ≈ 7° predicted between metallic and

charge-ordered states (Fig. 1G) is expected to provide further nanoresolved optical contrast to the insulator-metal transition.

Near-field optical properties

First, we present data obtained from a homogeneous α-(BEDT-TTF)₂I₃ single crystal. Figure 2A displays a 28 μm by 28 μm spot of the near-field amplitude β recorded close to the CO transition with a spatial resolution of 25 nm. There is a well-defined phase boundary between the metallic (yellow) and insulating (red) regions, providing evidence for the first-order nature of the CO transition in α-(BEDT-TTF)₂I₃. To obtain reliable absolute values of β, we normalized the scale to the near-field intensity of a thin gold layer evaporated onto the surface of the crystal in the vicinity of the surface region under study. From the histogram distribution of optical response amplitudes among pixels in the mapped area, the charge-ordered part of the image with a near-field amplitude about β = 0.5 can be distinguished from the metallic region, where β = 0.65. The larger contrast is in good agreement with calculations according to Eq. 1. The corresponding optical phase φ of the near-field response (Fig. 2B) also shows distinguishable metallic and charge-ordered regions perfectly overlapping with the amplitude data in Fig. 2A. The corresponding maxima are well separated and occur at 3° and 12°, respectively. There is essentially no phase difference noticeable between the charge-ordered regions of α-(BEDT-TTF)₂I₃ and the gold layer, the border of which is indicated by the dotted white line in Fig. 2B. The more inductive response of the metallic phase, likely a result of low plasma frequency, produces the relative contrast at these energies.

Upon changing temperature, the border between the phases propagates quickly across the specimen and, within a few hundred millikelvins, moves out of the observation window. The crystal is glued to a heat sink several hundred micrometers away from the gold edge in the top left corner. It seems that radiation absorption from the probing laser ($P \approx 0.5$ mW) heats up the crystal, thus creating a local

temperature gradient. For that reason, the transition occurs only 3 K below the nominal transition temperature of 136 K. The small co-existence range of a few hundred millikelvins is in good accordance with literature (*17*) and indicates high sample quality with an essentially uniform transition temperature.

Spatially modulated CO transition in topographically nonuniform samples

In the next step, we have conducted nanoimaging of the CO transition in topographically nonuniform, multiply cracked α-(BEDT-TTF)$_2$I$_3$ samples, which consist of many loosely connected crystallites of different sizes and shapes. This way, we can spatially resolve the evolution of the border between metallic and insulating regions, as well as their modulations tied to an inhomogeneous internal strain environment. The experimental conditions simulate very well a scenario of limited sample quality with intergrown crystallites, potentially introduced by improper mounting, which may lead to inconclusive macroscopic measurement results. Note that, in some materials, even internal stress upon a phase transition can cause fracturing of single crystals, which required using thin films in the case of VO$_2$, for instance, where structural changes between the metallic and insulating phases can be detrimental to crystal integrity (*8*). Exploring chemically clean but topographically non-uniform samples, therefore, provides the opportunity to study the effects of internal strain on a quantitative level.

A 40 μm by 40 μm area of the specimen that includes the gold reference on the right where the crystal was also thermally anchored was selected. In Fig. 3A, several images that were recorded in small temperature steps when cooled down below the nominal transition at T_{CO} = 136 K are displayed. In the upper part, flakes can be identified, which are disconnected from the main crystallite by cracks. In the main area, we see that the charge-ordered phase successively grows upon cooling, starting from the gold layer where the minimum temperature is expected, but even down to $T \leq 130$ K, stripe-like metallic relicts persist in the bottom part of the map. Phase coexistence over such a large temperature range cannot be explained just by temperature gradients. Despite the rapidly vanishing electrical conductivity, the thermal conductivity merely changes at the phase transition—a 25% drop was reported in (*32*)—due to the large phononic contribution, which rules out temperature gradients of 5 K within a few micrometers.

For a more quantitative analysis, we evaluated the pixel distributions of the largest single segment; the other regions and the area covered with gold were masked, as indicated by blue color in the 132.15 K map of
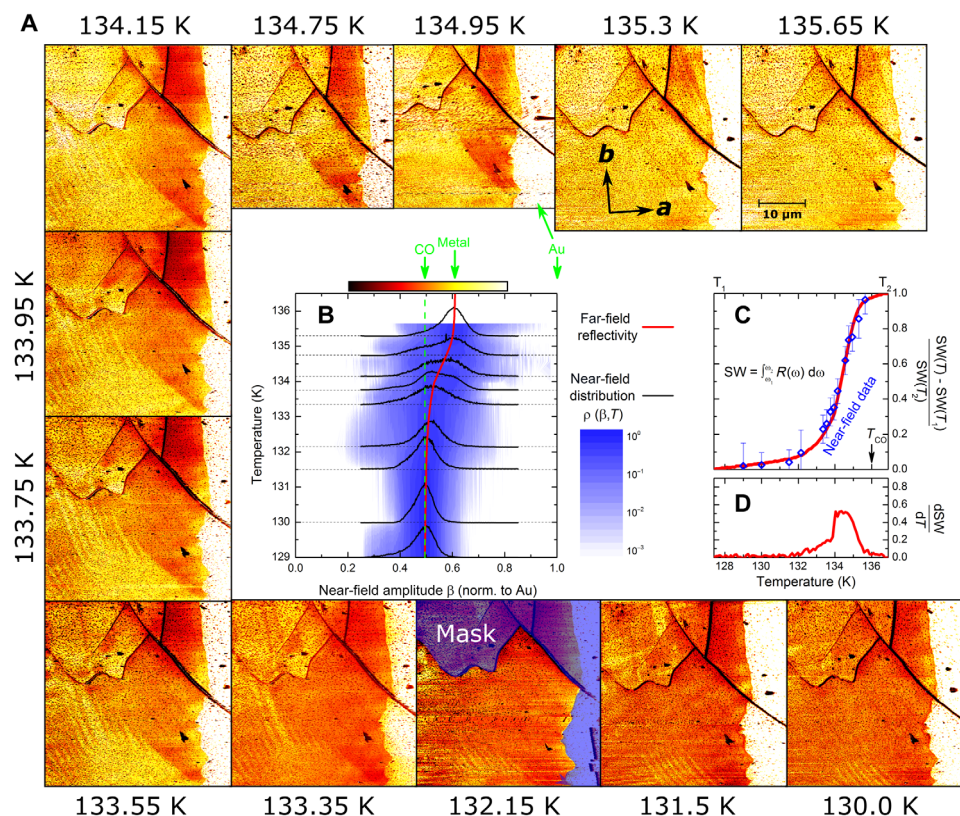

Fig. 3. Near-field maps of a multiply cracked α-(BEDT-TTF)$_2$I$_3$ crystal. (A) Near-field nanoimages taken at different temperatures close to T_{CO} = 136 K. A phase separation occurs between metallic (yellow) and insulating (red) regions, with a phase coexistence over a temperature range $\Delta T \leq 6$ K. The near-field amplitude β was normalized to the signal taken off a 30-nm gold layer (bright region on the right) evaporated beforehand. **(B)** To quantitatively analyze the temperature evolution of the two phases, we determined the pixel distribution ρ(β) of a well-defined region, which is indicated in the 132.15 K frame by masking (blue) the gold pad or separated flakes. The contour plot and black lines correspond to the amplitude distribution at the measured temperatures. In the temperature range with the largest changes (between 133.5 and 135 K), a bimodal distribution is observed, indicating the coexistence of metallic and charge-ordered regions. The trend follows the result of our subsequent far-field experiments (red line) on the same area. **(C)** The far-infrared reflectivity was integrated, as indicated in Fig. 1D, and the resulting temperature-dependent spectral weight (SW) was normalized to the high- and low-temperature (T_2 and T_1, respectively) plateau values. The temperature dependence of the average near-field intensity from (B) shows perfect correspondence to the far-field data. **(D)** The derivative of the SW with respect to temperature was calculated to highlight the largest rate of change. Figure reproduced from (*55*).

Fig. 3A. Figure 3B displays the near-field amplitude histogram at different temperatures. At the highest and lowest temperatures investigated, singular peaks that identify the metallic and charge-ordered insulating phases are seen. For the temperature range of strongest amplitude changes, however, a double-peak structure is found in accordance with the observed bimodal phase coexistence. The subsequent far-field reflectivity measurements plotted in Fig. 3 (C and D) exhibit a good agreement with the temperature evolution in amplitude of the average near-field response. Probing different spots on the crystal surface reveals distinct temperature dependence for those parts of the sample that exhibit the transformation at different temperatures; both the transition temperature T_{CO} and the width of the transition vary with position (see the Supplementary Materials).

The thermal behavior of the phase boundary can be investigated by determining its motion as the temperature is varied. To that end, we measure the distance d of the borderline to a fixed point, such as the crack indicated by the green double-headed arrow in Fig. 4A; the temperature dependence of d is plotted in Fig. 4D. Initially, the insulating phase expands rather quickly when T drops below T_{CO}, consistent with a realistic temperature gradient of several kelvins per millimeter. This appears rather large, but the small sample thickness of $d = 15$ μm and the cracks hinder heat transport comparable to single crystals. Below 134.5 K, however, the phase boundary propagates much more slowly and the equivalent temperature gradient rises to $dT/dx \approx 80$ K/mm (Fig. 4D), ruling out any thermometric origin.

The most stunning observation on the CO transition is the appearance of a pronounced "zebra" pattern of stripes that are present over large areas more or less in the complete temperature range reported here. We performed a more detailed scan at 133.95 K and present the corresponding 10 μm by 10 μm near-field map with a resolution of 20 nm in Fig. 4B. From the line cut (Fig. 4C), the periodicity of the stripes is determined as 2 μm. The boundaries between the metallic and insulating regions of the stripes have a width of several hundred nanometers. We contextualize this observation by noting that spontaneous development of stripe-like domains has been observed in other physical systems when the phase transition is coupled to strain while geometrically confined (33). Similar observations have been reported for VO$_2$ microcrystals subject to stress from a substrate (34), as well as in strained VO$_2$ thin films epitaxially clamped to TiO$_2$ substrate, in which a stripe-like morphology of metallic domains emerged close to the Mott-Peierls metal-insulator transition (4). Moreover, a spontaneous morphology of bidirectional stripes was resolved by low-temperature nanoimaging through the Mott metal-insulator transition of the related compound V$_2$O$_3$ (5). The common feature to these transitions is the presence of an accompanying structural transformation that induces a change in size and shape of the unit cell, which is frustrated by epitaxial clamping in the case of aforementioned oxide thin films. In addition, the material discussed here is subject to a nontrivial structural modification at the CO transition: α-(BEDT-TTF)$_2$I$_3$ exhibits a contraction along the a direction, while the b axis expands upon cooling through T_{CO} (19). These factors reveal a fundamental coupling between strain and the CO transition that can explain our results—the first reported observation by low-temperature nano-optical imaging of spontaneous striped insulator-metal coexistence in a phase-change crystal.

To rationalize the unique spatial morphology emerging from the metal-insulator transition in this α-(BEDT-TTF)$_2$I$_3$ crystallite segment, we propose a phenomenological Landau theory that accounts for both thermal properties of the CO transition and its coupling to strain. Therefore, we introduce an order parameter ψ whose value reflects
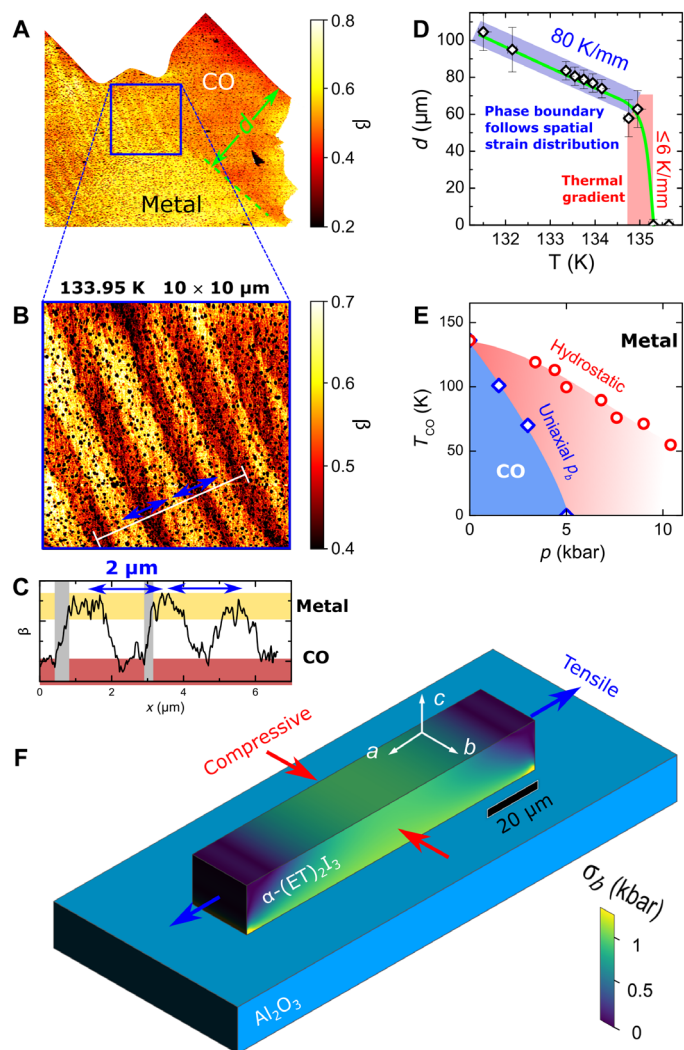
Fig. 4. Spatial variation of CO. (**A**) Optical near-field map of the α-(BEDT-TTF)$_2$I$_3$ crystal at $T = 133.95$ K. The green double-headed arrow indicates the distance d of the metal-insulator boundary (dashed green line) with respect to the top right crack. The blue frame corresponds to the 10 μm by 10 μm area magnified in (**B**) with a high spatial resolution of 20 nm. A pronounced pattern is seen with basically parallel lines of alternating metallic and insulating regions of approximately equal width. The blue double-headed arrows illustrate the periodicity. (**C**) The intensity profile recorded along the white line in (B) reveals a stripe periodicity of 2 μm and a phase boundary width of few hundred nanometers (gray). (**D**) The distance d between the crack and the metal-insulator phase boundary, illustrated in (A), was determined at several temperatures. When T falls below T_{CO}, a large area parallel to the crack becomes charge ordered within a fraction of a kelvin (≤0.35 K). This quick propagation of the phase boundary is attributed to a temperature gradient smaller than 6 K/mm. Below 134.5 K, the metallic phase retreats at a much slower rate, implying that the effect is not caused by a temperature gradient. (**E**) Pressure-dependent studies reveal that uniaxial strain along the b axis more efficiently suppresses CO than hydrostatic compression [T_{CO} data taken from (28, 29)]. Comparison with near-field data from our experiments estimates an effective uniaxial pressure $p_b \approx 0.5$ to 1 kbar on the α-(BEDT-TTF)$_2$I$_3$ sample under investigation. (**F**) Attaching the sample at both ends and cooling on a sapphire substrate imposes tensile strain along the a axis and compression along b due to differential thermal contraction. The calculated strain profile upon tensile stress reveals large strain at the center of the segment and small values close to the edges. Figure reproduced from (55).

the amplitude of local charge disproportion: $\psi(\vec{r}) > 0$ implies the onset of CO at location $\vec{r}$ within the crystal, and the equilibrium configuration $\psi_{eq}(\vec{r})$ at constant temperature minimizes the Landau free energy $F[\psi(\vec{r}), T] = \int_V d^3 r f(\psi, T)$, integrated over the crystal volume V at constant temperature T. This formalism approximates the volumetric Landau free energy density f in powers of ψ

$$f = f_{CO}(\vec{r}) + f_{DW}(\vec{r}) + f_\varepsilon(\vec{r}) \qquad (2)$$

with the three contributions

$$f_{CO}(\vec{r}) \equiv D(\vec{r})\psi(\vec{r}) + \alpha(T - T_{CO})\psi^2 - \beta\psi^3 + \gamma\psi^4 \qquad (3)$$

$$f_{DW}(\vec{r}) \equiv \frac{1}{2}\kappa|\nabla\psi|^2, \text{ and } f_\varepsilon(\vec{r}) \equiv -\frac{1}{2}\underline{\varepsilon}(\vec{r}) : \underline{K} : \underline{\varepsilon}^*\psi(\vec{r}) \qquad (4)$$

The first term f_{CO} of the free energy represents the temperature-dependent specific free energy of the charge-ordered phase, whose present "double well" form induces the first-order transition from metal ($\psi = 0$) to insulator ($\psi > 0$) upon cooling to $T < T_{CO}$, thereby reproducing the nanoscale phenomenology of a first-order CO transition reported here in Fig. 2. Here, α, β, and γ are positive coefficients of the Landau theory whose values are fixed (up to an overall constant) by the value of ψ in the charge-ordered phase and by the hysteresis width of the thermal transition. A disorder potential $D(\vec{r})$ within the crystal, as generated, e.g., by crystallographic or chemical defects, is presumed to couple to the CO parameter ψ.

Next, f_{DW} represents the energetic contribution of domain walls between charge-ordered insulator and metallic domains, where κ crucially denotes the energy per unit area of domain boundaries. Last, f_ε represents the coupling of the order parameter to the lattice, whereby the transition to the homogeneous CO phase tends to reconfigure the unit cell to a state of "spontaneous strain" described by the second-rank strain tensor $\underline{\varepsilon}(\vec{r})$ tending toward $\underline{\varepsilon}^*$ and $\underline{K}$ denotes the associated (fourth rank) stiffness tensor (note that $\ldots : \underline{K} : \ldots$ denotes the tensor inner product). This form of f_ε can be derived for the case of an elastically clamped crystal undergoing a structural phase transition (see the Supplementary Materials). Heidmann et al. (19) identified the structural change accompanying CO in α-(BEDT-TTF)$_2$I$_3$ as a dilatation. In this case, the spontaneous strain is a diagonal tensor: $\varepsilon_{ii}^* \equiv \Delta\alpha_i/\alpha_i \approx (-1, +1, -0.3) \times 10^{-3}$ for crystallographic axes $i = a$, b, and c, with α_i as the associated lattice constant.

We first demonstrate that two essential features of Eqs. 3 to 4 conspire in the present model to reproduce the phenomenology of stripe-like domain morphology in proximity to T_{CO}. Since the form of f_ε in Eq. 4 follows from geometric confinement of the crystal upon a clamping substrate, homogeneous strains of the crystal are energetically disfavored, and the coupling $\underline{\varepsilon}(\vec{r}) : \underline{K} : \underline{\varepsilon}^*\psi(\vec{r})$ instead predisposes $\psi_{eq}(\vec{r})$ toward a shape instability of comparably lower energy, as shown in the Supplementary Materials. In the present case, this instability takes the form of stripes perpendicular to the crystal a axis with a characteristic periodicity as small as ζ (compare the Supplementary Materials for more details)

$$\zeta \equiv \frac{2\pi\sqrt{1+\nu}}{|\Delta\alpha_a/\alpha_a|}\frac{1-2\nu}{1-\nu}\sqrt{\frac{\kappa}{E}}. \qquad (5)$$

Here, ν and E represent the in-plane Poisson's ratio and Young's modulus of α-(BEDT-TTF)$_2$I$_3$, respectively (35). Equation 5 thus reflects energetic competition between the "smoothing" tendencies of domain boundary stiffness κ and the "coarsening" effect of accommodating mismatched structural phases within a confined crystal volume. In this model, the balance of domain wall energies against the dense accommodation of elastically mismatched phases ultimately determines the texture and wavelength of phase coexistence. With similar phenomenology, we have discovered that elastically confined α-(BEDT-TTF)$_2$I$_3$ joins the ranks of other correlated electron materials that exhibit patterned phase coexistence through an insulator-metal transition (4, 36). Crucially, this implies that the spatial character of phase coexistence in α-(BEDT-TTF)$_2$I$_3$ encodes details of the microscopic energetics controlling the CO transition, including the coupling between CO and strain.

With regard to strain coupling, a second phenomenology is necessary to fully explain our observations in the present α-(BEDT-TTF)$_2$I$_3$ crystallite. We now consider the rationale for nucleation and initial growth of the CO phase at the crystallite's outermost edges, in close proximity to cracks. We propose that the enormous thermal contraction of the crystal causes large tensile stress, which strongly suppresses the metal-insulator transition (28) in the following way. The α-(BEDT-TTF)$_2$I$_3$ specimen exhibits a considerably larger thermal expansion coefficient compared to the sapphire substrate (19, 37, 38) to which it is affixed by epoxy lengthwise along the crystal a axis. Thus, this sample experiences strong tensile stress along the a direction, accompanied by a compression in the perpendicular b and c directions on account of volume conservation (in other words, the nonzero Poisson's ratio ν), as depicted schematically by the crystallographically aligned arrows indicated in Fig. 4F. Upon cooling from room temperature toward the CO transition, the crystal fractures as a result, subdividing into many segments. Intuitively, the resulting crystallite edges are regions in which strain has been relieved by the crack formation, whereas the crystal interior remains under a state of inhomogeneous strain.

Heuristically, the aforementioned coupling of the CO transition to a structural transformation implies that tensile strain along the a axis favors the metallic state, for its lattice constant is larger in the metallic than in the CO phase. Figure 4F presents the results of a quasi–two-dimensional simulation looking at the ac plane of the crystalline bar mechanically clamped at the ends; as seen from the false color presentation, the compressive strain in the b axis develops inhomogeneously. Uniaxial compressive strain along the b direction is reportedly much more effective in suppressing CO than hydrostatic pressure (29, 39). Detailed structural investigations under uniaxial pressure revealed that the wave function overlap between the BEDT-TTF sites increases more strongly for the b axis pressure (p_b) as compared to the a axis or hydrostatic pressure. In particular, the enhancement of intermolecular transfer integrals t_i is most pronounced between sites A and C, as well as between sites B and C (compare Fig. 1, B and C) (38), thus diminishing the effective correlations V/W; the electronic bandwidth ($W \propto \Sigma t_i$) along the direction of alternating charges increases more strongly than the intersite Coulomb repulsion V. This behavior stems, most likely, from a change of the dihedral angle between the organic molecules within the conducting layers, similar to the θ-(BEDT-TTF)$_2$X family (40). In Fig. 4E, we compare the variation of T_{CO} by uniaxial p_b and hydrostatic pressure. With this effect, we can explain how the CO transition temperature is reduced toward the center of the crystallite and why the effects of thermally induced strain in this sample are particularly pronounced. The coexistence regime of $\Delta T_{CO} \leq 6$ K

corresponds to an equivalent pressure along the b direction of approximately 0.5 kbar.

We now combine the phenomenology of stripe morphology and the spatially nonuniform suppression of the CO transition, taking both within the context of the Landau theory (Eq. 2). In this case, we subdivide the stress tensor $\mathcal{S}(\vec{r}) \equiv \underline{K} : \underline{\varepsilon}(\vec{r})$ into two contributions. The first part is a background stress field S_b as displayed in Fig. 4F associated with clamping of the crystal to the sapphire substrate with dissimilar coefficient of thermal expansion. The remaining strain field stems from the inhomogeneous distribution of $\psi(\vec{r})$ and must be predicted self-consistently (see the Supplementary Materials). We then compute an equilibrium configuration $\psi_{eq}(\vec{r}, T)$ at incremental temperatures close to T_{CO} via global numerical minimization of Eq. 2 within the same quasi–two-dimensional crystallite volume displayed in Fig. 4F. We heuristically quantify the corresponding distribution of metallicity by $1 - \psi(\vec{r})$ and present the result in Fig. 5A for a variety of temperatures when T is raised through T_{CO}. The progression of the metallic phase starts from the crystal center and expands toward the cracked edges. The simulations very much resemble the nanoimaging results presented in Fig. 3, including especially the bifurcation of the metallic state boundaries into a zebra-patterned morphology of alternating CO/metallic stripes oriented perpendicularly to the a axis of the crystal. Note that, in addition to the intrinsic material properties, the stripe periodicity depends on the magnitude and direction of the strain; in addition, for other samples, we observed qualitatively similar patterns (Fig. 6E) but with different length scales.

In addition to evaluating the phase boundary, we obtain direct insight into the internal strain distribution within a completely charge-ordered area by considering the absolute values of the near-field amplitude. Figure 5B displays variations of the near-field amplitude β within an insulating region. From pressure-dependent dc transport and optical data (28–30) presented in Fig. 5 (C to E), it becomes evident that

the charge gap is successively narrowed with pressure. This manifests in the spectral response as a continuous increase of the optical conductivity. Upon closely inspecting the amplitude of the near-field optical response in the insulating area, we notice that it drops considerably toward the top right edge, as revealed by the intensity profile along the white line in Fig. 5B. We attribute the reduction of conductivity to a gradual enlargement of the energy gap Δ_{CO} due to a reduction in S_b toward complete b axis strain relief at the crystal edges. This observation is in excellent agreement with the calculated strain profile displayed in Fig. 4F, demonstrating that a gradient of the b axis strain is expected to exceed 1 kbar, even in a microscopic region of the sample. Thus, our cryogenic near-field experiments reveal sensitivity to a local modulation of the electronic correlation strength V/W on a micrometer length scale evoked by spontaneous inhomogeneous strain.

DISCUSSION
Using our recently developed cryo-SNOM, we have conducted low-temperature near-field optical investigations on α-(BEDT-TTF)$_2$I$_3$ single crystals to elucidate the nanoscale spatial distribution of charge ordering transpiring at the metal-insulator transition $T_{CO} = 136$ K. For a homogeneous single crystal, our experiments reveal a sharp transition; we detect a developed phase boundary that originates from a small thermal gradient on the sample ($dT/dx \approx 5$ K/mm). Our findings unequivocally demonstrate the first-order nature of the CO transition in α-(BEDT-TTF)$_2$I$_3$, as illustrated in Fig. 6 (A and D).

When the specimen is clamped on a substrate and subject to pronounced internal strain, nonuniformly relieved at the location of multiple cracks, the crystal enters an intrinsic regime of spatially inhomogeneous phase coexistence and exhibits a qualitatively different behavior. Metallic and charge-ordered regions spatially coexist in a broad temperature interval, generally suppressing the metal-insulator
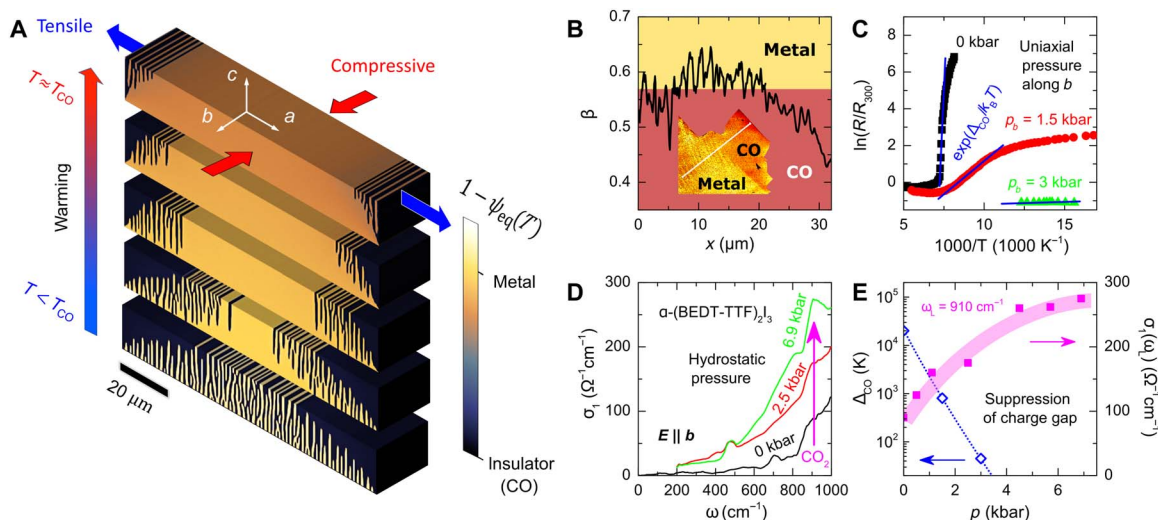

Fig. 5. Strain dependence of the charge gap. (**A**) The interplay of metallic and charge-ordered phases is simulated at different temperatures throughout the phase transition. Very similar to the experimental data from Figs. 3A and 4 (A to C), CO successively grows from the edges of the segment, while the metallic phase is repressed toward the center, forming a characteristic stripe pattern. (**B**) A line cut of the near-field amplitude (along the white line in the inset) reveals reduced signal at the edges of the segment compared to its center. (**C**) The Arrhenius plot of the temperature-dependent resistance allows extracting the energy gap Δ_{CO} at different uniaxial pressures applied along the b axis [data taken from (29)]. (**D**) In addition, the hydrostatic pressure shifts the metal-insulator transition, weakens CO, and thus suppresses the spectral gap [data taken from (30)]. (**E**) Consistently, the transport gap Δ_{CO} determined from (C) is reduced with pressure as well. At the CO$_2$ laser frequency of 910 cm^{-1}, the optical conductivity is gradually enhanced with pressure. Therefore, the drop of near-field intensity in (B) indicates a larger optical gap due to smaller strain close to the edges, imposing a local modulation of the correlation strength.
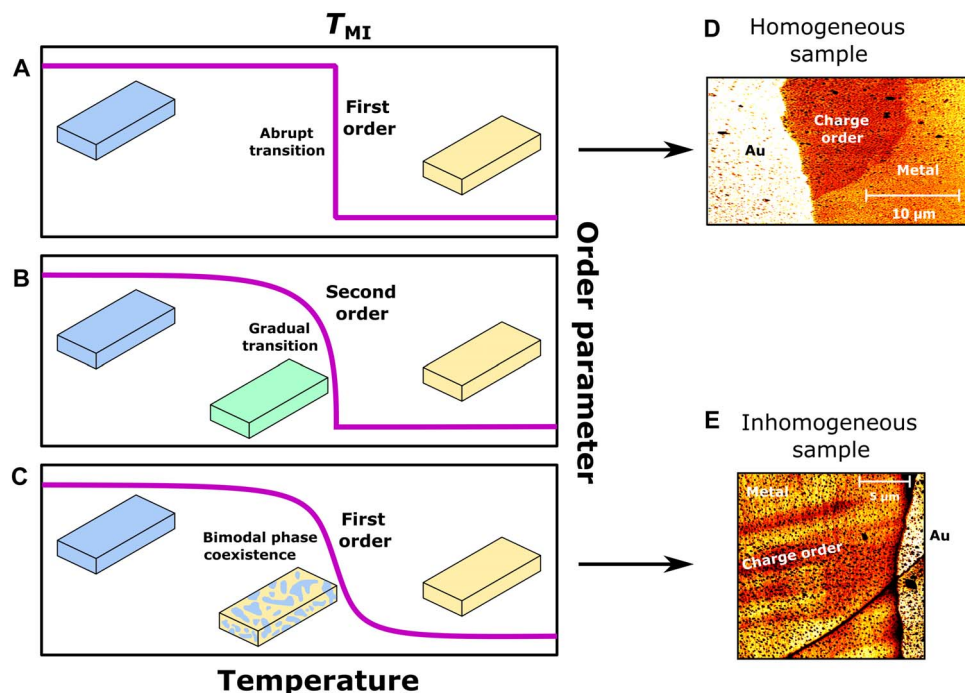
Fig. 6. Possible scenarios of metal-insulator transitions in solids. A general distinction can be made between (**A**) abrupt first-order phase transitions and (**B**) gradual mean-field–like second-order transitions. (**C**) In the case of a bimodal phase coexistence of an originally first-order transition, the macroscopic order parameter looks very similar to the second-order scenario. Such a spatial phase separation may be the result of a nonuniform field caused by internal strain or defects that couple energetically to the relevant order parameter. At T_{CO}, we observe differences in the optical near-field maps of samples with distinct characteristics. (**D**) Homogeneous α-(BEDT-TTF)$_2$I$_3$ single crystals exhibit a well-defined phase boundary that follows the temperature gradient on the sample. Upon proper thermalization, the macroscopic transition happens instantaneously (within a few hundred millikelvins) on the whole crystal, similar to that in Fig. 2. (**E**) In geometrically nonuniform samples, the internal strain spatially modulates electronic correlations, resulting in a complex phase coexistence that extends over several kelvins (compare Fig. 3). Figure reproduced from (*55*).

transition toward lower temperatures. We identify local modulations of strain within a single-crystal segment, which physically manifest the same consequences as uniaxial pressure. Thus, strain is relieved in the regions close to the segment boundary, i.e., the crack, whereas the effective pressure is largest in the center. As a result, the metallic phase persists more than 6 K below the nominal transition temperature corresponding to uniaxial pressure of approximately 0.5 kbar. The material reacts to this external stimulus and minimizes buildup of elastic strain via spontaneous formation of stripes perpendicular to the direction of strain. The quantitative details of the observed zebra morphology, including the periodicity ζ, width, and sharpness of stripes, directly reflect the competition of domain boundary stiffness and elastic energy in the crystal, as elaborated in Eq. 5. To that end, applying strain along a different crystal axis results in a qualitatively similar stripe modulation aligned perpendicularly to the direction of strain yet with different periodicity and temperature range.

The local optical probe provides us with the unique opportunity to directly monitor the spatially modulated first-order phase transition (Figs. 3 and 6E), which would show up as a broad crossover (Fig. 6C) in a bulk measurement, broadly indistinguishable from a second-order transition (Fig. 6B). We point out potential applications in materials science, such as characterization and identification of novel phases of matter in inhomogeneous samples, even before clean single crystals are available. Moreover, we provide evidence for a spatial modulation of the electronic correlation strength originating spontaneously from an underlying distribution of strain. The discovered zebra-like stripe patterns of phase coexistence are expected to be present in other strong-

ly correlated electron systems where a (e.g., magneto-/ferroelastic, Jahn-Teller, or Peierls-like) coupling to the lattice exists. This opens a new avenue for experimental studies and control of microscopically phase-separated systems and calls for further theoretical and nanoimaging investigations among other prototypic correlated electron solids.

Note that the data here are acquired on bulk single crystals, providing a much cleaner evaluation of the local correlation strength as compared to thin films. The VO$_2$ thin films (thickness, 100 nm) studied in (*8*) show a grain size of order 50 to 100 nm. This is similar to the puddle size of metallic regions, which can thus be linked to the thin film inhomogeneity. Comparative studies on VO$_2$ bulk single crystals indeed proved that the complex pattern of phase coexistence in thin films is related primarily to epitaxial strain gradients (*4*). It is therefore desirable to study the intrinsic behavior of correlated electrons upon metal-insulator transitions in the absence of these structural effects. We suggest to explore the spatial properties of genuine Mott insulators in single-crystalline molecular conductors of the κ-(BEDT-TTF)$_2X$ family at low temperatures in the vicinity of the first-order transition. Here, dynamical mean-field theory predicted an extended phase coexistence region (*41*), which was recently substantiated by first experimental evidence (*42*, *43*). Previous far-field optical studies on κ-(BEDT-TTF)$_2$Cu[N(CN)$_2$]Br mapped the spatial phase segregation between the metallic state and the antiferromagnetic Mott insulator (*23*, *24*). Yet, this work used vibrational features to discriminate between metal and insulator, not probing the electronic response directly, and the resolution was confined to the diffraction limit of infrared radiation ($\approx$10 μm). Cryogenic nanoimaging provides a straight route to disclose the

nanoscale evolution of the correlated metal out of the Mott-insulating state, particularly allowing us to probe the spectral properties of coherent quasiparticles within the metallic puddles. Most intriguing is the case of quantum spin liquids that allow investigating the direct transition from the Mott insulator to the Fermi liquid in the absence of magnetic order (42, 43).

Our explorative study demonstrates the particular strength of near-field optical microscopy for resolving the interplay of metallic and insulating phases of correlated electron systems, especially at low temperatures. In principle, this method is not limited to probing the opening of a spectral gap, but—using other light sources—it can be applied in a similar way to phonons and vibrations [compare the far-field results in (23, 24)], as well as other characteristic features that exhibit pronounced changes in optical conductivity. In this direction, further experiments on the charge-sensitive vibrations in α-(BEDT-TTF)$_2$I$_3$ are underway, which are in principle also susceptible to the domain walls suggested in relation to the ferroelectric response (17), as previously substantiated in quasi–one-dimensional (TMTTF)$_2$X (18).

With these possibilities at hand, it becomes feasible to scrutinize the nanoscale evolution of electronic crystal growth in the time domain—at least for processes on larger time scales than the measurement. In particular, cooling rate–dependent studies on frustrated CO systems have recently suggested a complex phase coexistence with intermediate domains between the metallic and charge-ordered state (44). Assessing the spectral information of both electronic and vibrational features would allow distinctively assigning the local nature of the electronic state.

METHODS

Sample preparation

α-(BEDT-TTF)$_2$I$_3$ single crystals were grown by D. Schweitzer using standard electrochemical methods (45). Single crystals are plate like, with lateral dimensions of several millimeters and thickness $d \approx 10$ to 100 μm. We first preselected samples with clean surfaces, judging from their visual appearance under an optical microscope. In a next step, AFM images of the crystal surfaces were taken, yielding a typical roughness of 5 to 10 nm for good samples. The surface topography does not coincide with the characteristic phase boundary detected by near-field optics. This fact is taken as another strong evidence that our optical measurements probe the bulk properties; these are affected by electronic correlations under inhomogeneous strain but are not related to surface impurities or defects. In situ AFM maps of the crystal surfaces displayed in Figs. 2 and 3 are presented in fig. S1.

The selected high-quality specimens were then mounted on sapphire substrates using a conductive carbon paste. Apart from electrical transport and its mechanical properties, this type of glue has a good thermal conduction that effectively dissipates heat away from the sample during the gold evaporation procedure. Shadow masks were individually manufactured from a thin metallic foil and arranged close to the sample surface for the gold deposition. The entire substrate was fixed in a vacuum chamber about 50 cm above the boat. Such a long distance is necessary for two reasons: Placing the specimen far away from the boat effectively reduces heating effects, and it geometrically supports the deposition of sharp gold edges with a step height of 30 to 40 nm and a width of <1 μm (fig. S1), as required for the near-field experiments. Evaporation was performed at a slow rate of 2 Å to reduce heating of the crystal. Mon-itoring and regulating the sample temperature are crucial because organic charge-transfer salts become unstable just a few hundred kelvins above room temperature. When exposed to elevated temperatures for a longer period of time, the compound is known to lose iodine; α-(BEDT-TTF)$_2$I$_3$ may also change phase upon moderate tempering around 80°C (46). For that reason, we again checked the optical properties subsequent to the gold evaporation and verified that the material properties were not altered.

Cryogenic optical near-field experiments

For near-field experiments, the sapphire substrates were mounted on the sample holder via a conductive silver paste that acts as a good heat conductor as well. When the glue had dried, the sample holder was inserted into a quick-entry load lock for entry into the ultrahigh vacuum (10^{-10} mbar) environment of the microscope chamber. After insertion to the sample holder, the sample was cooled to low temperature by a flexible copper braid connected to a liquid helium flow cryostat (Janis Research Company); precise temperature control is afforded by an integrated heater and temperature sensor (silicon diode) operated with a temperature controller (Lake Shore Cryotronics). At each temperature of interest, the sample was micropositioned and raster scanned (attocube micropositioning hardware) below the sharp probe tip of the integrated AFM, which is operated in noncontact feedback. Coherent radiation from a CO_2 gas laser (910 cm^{-1} ≈ 113 meV) was directed through an infrared-transparent ZnSe window in the microscope chamber to an off-axis parabolic mirror micropositioned to focus directly onto the metallized tip of the AFM probe. Back-scattered radiation associated with the localized (<20 nm resolved) probe-sample near-field interaction (compare the sketch in Fig. 1F) was collimated by the same optic, detected outside the chamber at a liquid nitrogen–cooled mercury cadmium telluride photodetector and discriminated by pseudoheterodyne interferometry (47). More details on the technical realization of near-field spectroscopy in cryogenic circumstances can be found in (3, 4, 9), for instance.

The sample was cooled in the microscope at a rate of 1 K/min from room temperature down to 140 K, and the last few kelvins above T_{CO} were ramped slowly (0.05 K/min) to avoid undershooting the transition. Sample resistance was monitored in situ to establish the transition temperature. After reaching each temperature set point, the temperature was stabilized for approximately 5 min to ensure thermal equilibrium on the sample before initiating each near-field measurement (typically 500 by 500 pixels), requiring about 2 hours for each map. Near-field maps of several single crystals were recorded with typical results, as presented in Figs. 2, 3, and 6 (D and E).

Far-field experiments

After the near-field experiments have been finished, the samples were characterized by Fourier-transform infrared spectroscopy in far-field geometry. To that end, we used a coldfinger microcryostat in combination with an infrared microscope. The spatial resolution of ≈30 μm by 30 μm enabled us to identify and scrutinize the very same spot on the sample as investigated in near-field. Temperature was ramped with 1 K/min to a value slightly above the CO transition at $T_{CO} = 136$ K, and a spectrum was recorded for sample and reference mirror separately to determine the absolute reflectivity. Then, optical spectra in the mid-infrared (500 to 8000 cm^{-1}) were monitored on a selected area in intervals of 1 min during very slow cooling (0.01 K/min). By integrating the optical reflectivity in the range of 700 to 1000 cm^{-1} as indicated in

Fig. 1D, we determined the spectral weight SW(T) with a temperature resolution of 0.01 K, the result of which is plotted in Fig. 3 (C and D). This quantity measures the sum of insulating and metallic regions and thus serves as a kind of order parameter to trace the transition in a quantitative manner. We performed similar temperature sweeps through the transition at different spots of the surface, yielding distinct results indicative of regions with different strain, as discussed in the Supplementary Materials (48–54).

SUPPLEMENTARY MATERIALS

Supplementary material for this article is available at http://advances.sciencemag.org/cgi/content/full/4/12/eaau9123/DC1

Section S1. Sample preparation
Section S2. Optical far-field experiments
Section S3. Landau free energy calculations
Fig. S1. AFM profile of the sample surface.
Fig. S2. Far-field reflectivity on different spots of the cracked sample.
Fig. S3. Temperature-dependent far-field experiments.
Fig. S4. Schematics of the geometry used to treat the elasticity problem.

REFERENCES AND NOTES

1. H. E. Stanley, *Introduction to Phase Transitions and Critical Phenomena* (Oxford Univ. Press, 1971).
2. E. Dagotto, Complexity in strongly correlated electronic systems. *Science* **309**, 257–262 (2005).
3. J. M. Atkin, S. Berweger, A. C. Jones, M. B. Raschke, Nano-optical imaging and spectroscopy of order, phases, and domains in complex solids. *Adv. Phys.* **61**, 745–842 (2012).
4. M. K. Liu, A. J. Sternbach, D. N. Basov, Nanoscale electrodynamics of strongly correlated quantum materials. *Rep. Prog. Phys.* **80**, 014501 (2017).
5. A. S. McLeod, E. van Heumen, J. G. Ramirez, S. Wang, T. Saerbeck, S. Guenon, M. Goldam, L. Anderegg, P. Kelly, A. Mueller, M. K. Liu, I. K. Schuller, D. N. Basov, Nanotextured phase coexistence in the correlated insulator V₂O₃. *Nat. Phys.* **13**, 80–86 (2016).
6. E. Dagotto, *Nanoscale Phase Separation and Colossal Magnetoresistance: The Physics of Manganites and Related Compounds* (Springer-Verlag, 2002).
7. S. Liu, B. Phillabaum, E. W. Carlson, K. A. Dahmen, N. S. Vidhyadhiraja, M. M. Qazilbash, D. N. Basov, Random field driven spatial complexity at the Mott transition in VO₂. *Phys. Rev. Lett.* **116**, 036401 (2016).
8. M. M. Qazilbash, M. Brehm, B.-G. Chae, P.-C. Ho, G. O. Andreev, B.-J. Kim, S. J. Yun, A. V. Balatsky, M. B. Maple, F. Keilmann, H.-T. Kim, D. N. Basov, Mott transition in VO₂ revealed by infrared spectroscopy and nano-imaging. *Science* **318**, 1750–1753 (2007).
9. K. W. Post, A. S. McLeod, M. Hepting, M. Bluschke, Y. Wang, G. Cristiani, G. Logvenov, A. Charnukha, G. X. Ni, P. Radhakrishnan, M. Minola, A. Pasupathy, A. V. Boris, E. Benckiser, K. A. Dahmen, E. W. Carlson, B. Keimer, D. N. Basov, Coexisting first- and second-order electronic phase transitions in a correlated oxide. *Nat. Phys.* **14**, 1056–1061 (2018).
10. H. Seo, J. Merino, H. Yoshioka, M. Ogata, Theoretical aspects of charge ordering in molecular conductors. *J. Phys. Soc. Jpn.* **75**, 051009 (2006).
11. M. Dressel, M. Dumm, T. Knoblauch, M. Masino, Comprehensive optical investigations of charge order in organic chain compounds (TMTTF)₂X. *Crystals* **2**, 528–578 (2012).
12. A. Pustogow, T. Peterseim, S. Kolatschek, L. Engel, M. Dressel, Electronic correlations versus lattice interactions: Interplay of charge and anion orders in (TMTTF)₂X. *Phys. Rev. B* **94**, 195125 (2016).
13. X. Shao, Y. Nakano, M. Sakata, H. Yamochi, Y. Yoshida, M. Maesato, M. Uruichi, K. Yakushi, T. Murata, A. Otsuka, G. Saito, S. Koshihara, K. Tanaka, Room-temperature first-order phase transition in a charge-disproportionated molecular conductor (MeEDO-TTF)2PF6. *Chem. Mater.* **20**, 7551–7567 (2008).
14. Y. Yue, K. Yamamoto, M. Uruichi, C. Nakano, K. Yakushi, S. Yamada, T. Hiejima, A. Kawamoto, Nonuniform site-charge distribution and fluctuations of charge order in the metallic state of α–(BEDT-TTF)2I3. *Phys. Rev. B* **82**, 75134 (2010).
15. T. Ivek, R. Beyer, S. Badalov, M. Čulo, S. Tomić, J. A. Schlueter, E. I. Zhilyaeva, R. N. Lyubovskaya, M. Dressel, Metal-insulator transition in the dimerized organic conductor κ-(BEDT-TTF)₂Hg(SCN)₂ Br. *Phys. Rev. B* **96**, 85116 (2017).
16. M. Imada, A. Fujimori, Y. Tokura, Metal-insulator transitions. *Rev. Mod. Phys.* **70**, 1039–1263 (1998).
17. T. Ivek, B. Korin-Hamzić, O. Milat, S. Tomić, C. Clauss, N. Drichko, D. Schweitzer, M. Dressel, Electrodynamic response of the charge ordering phase: Dielectric and optical studies of α-(BEDT-TTF)₂I₃. *Phys. Rev. B* **83**, 165128 (2011).
18. R. Świetlik, B. Barszcz, A. Pustogow, M. Dressel, Raman spectroscopy evidence of domain walls in the organic electronic ferroelectrics (TMTTF)₂X(X = SbF₆, AsF₆, PF₆). *Phys. Rev. B* **95**, 085205 (2017).
19. C.-P. Heidmann, A. Barnsteiner, F. Grob-Alltag, B. S. Chandrasekhar, E. Hess, Anisotropic thermal expansion of the organic conductor α-(BEDT-TTF)₂I₃: New aspects of the metal-insulator transition. *Solid State Commun.* **84**, 711–716 (1992).
20. K. Yamamoto, A. A. Kowalska, K. Yakushi, Direct observation of ferroelectric domains created by Wigner crystallization of electrons in α-[bis(ethylenedithio)tetrathiafulvalene]₂I₃. *Appl. Phys. Lett.* **96**, 122901 (2010).
21. K. Katono, T. Taniguchi, K. Ichimura, Y. Kawashima, S. Tanda, K. Yamamoto, STM observation of charge stripein metallic phase of α-(BEDT-TTF)₂I₃. *Phys. Rev. B* **91**, 125110 (2015).
22. D. Lang, J. Döring, T. Nörenberg, Á. Butykai, I. Kézsmárki, H. Schneider, S. Winnerl, M. Helm, S. C. Kehr, L. M. Eng, Infrared nanoscopy down to liquid helium temperatures. *Rev. Sci. Instrum.* **89**, 033702 (2018).
23. T. Sasaki, N. Yoneyama, N. Kobayashi, Y. Ikemoto, H. Kimura, Imaging phase separation near the Mott boundary of the correlated organic superconductors κ-(BEDT-TTF)₂X. *Phys. Rev. Lett.* **92**, 227001 (2004).
24. T. Sasaki, N. Yoneyama, A. Suzuki, N. Kobayashi, Y. Ikemoto, H. Kimura, Real space imaging of the metal–insulator phase separation in the band width controlled organic mott system κ-(BEDT-TTF)₂Cu[N(CN)₂]Br. *J. Phys. Soc. Jpn.* **74**, 2351–2360 (2005).
25. F. Keilmann, R. Hillenbrand, Near-field microscopy by elastic light scattering from a tip. *Philos. Trans. A Math. Phys. Eng. Sci.* **362**, 787–805 (2004).
26. T. Taubner, F. Keilmann, R. Hillenbrand, Nanoscale-resolved subsurface imaging by scattering-type near-field optical microscopy. *Opt. Express* **13**, 8893–8899 (2005).
27. M. Lopes, C. M. Quintero, E. M. Hernández, V. Velázquez, C. Bartual-Murgui, W. Nicolazzi, L. Salmon, G. Molnár, A. Bousseksou, Atomic force microscopy and near-field optical imaging of a spin transition. *Nanoscale* **5**, 7762–7767 (2013).
28. R. Beyer, A. Dengl, T. Peterseim, S. Wackerow, T. Ivek, A. V. Pronin, D. Schweitzer, M. Dressel, Pressure-dependent optical investigations of α-(BEDT-TTF)₂I₃: Tuning charge order and narrow gap towards a Dirac semimetal. *Phys. Rev. B* **93**, 195116 (2016).
29. N. Tajima, A. Ebina-Tajima, M. Tamura, Y. Nishio, K. Kajita, Effects of uniaxial strain on transport properties of organic conductor α-(BEDT-TTF)₂I₃ and discovery of superconductivity. *J. Phys. Soc. Jpn.* **71**, 1832–1835 (2002).
30. W. Li, E. Uykur, C. Kuntscher, M. Dressel, Electronic correlations among the dirac electrons in α-(BEDT-TTF)₂I₃ unveiled by high-pressure optical spectroscopy, arXiv:1803.00755 (2018) .
31. A. S. McLeod, P. Kelly, M. D. Goldam, Z. Gainsforth, A. J. Westphal, G. Dominguez, M. H. Thiemens, M. M. Fogler, D. N. Basov, Model for quantitative tip-enhanced spectroscopy and the extraction of nanoscale-resolved optical constants. *Phys. Rev. B* **90**, 085136 (2014).
32. M. Matsukawa, K. Hashimoto, N. Yoshimoto, M. Yoshizawa, Y. Kashiwaba, K. Noto, Thermal conductivity in the *ab*-plane of the organic conductor α-(BEDT-TTF)₂I₃. *J. Phys. Soc. Jpn.* **64**, 2233–2234 (1995).
33. A. M. Bratkovsky, V. Heine, E. K. H. Salje, Strain effects, particularly in phase transitions. *Philos. Trans. Royal Soc. A* **354**, 2875–2896 (1996).
34. A. C. Jones, S. Berweger, J. Wei, D. Cobden, M. B. Raschke, Nano-optical investigations of the metal-insulator phase behavior of individual VO₂ microcrystals. *Nano Lett.* **10**, 1574–1581 (2010).
35. T. Ishiguro, S. Kagoshima, H. Anzai, Elastic property of tetrathiafulvalene-tetracyanoquinodimethane (TTF-TCNQ). *J. Phys. Soc. Jpn.* **42**, 365–366 (1977).
36. D. Liu, K. Ishikawa, R. Takehara, K. Miyagawa, M. Tamura, K. Kanoda, Insulating nature of strongly correlated massless Dirac fermions in an organic crystal. *Phys. Rev. Lett.* **116**, 226401 (2016).
37. W. M. Yim, R. J. Paff, Thermal expansion of AlN, sapphire, and silicon. *J. Appl. Phys.* **45**, 1456–1457 (1974).
38. R. Kondo, S. Kagoshima, J. Harada, Crystal structure analysis under uniaxial strain at low temperature using a unique design of four-axis x-ray diffractometer with a fixed sample. *Rev. Sci. Instrum.* **76**, 093902 (2005).
39. M. Maesato, Y. Kaga, R. Kondo, S. Kagoshima, Uniaxial strain method for soft crystals: Application to the control of the electronic properties of organic conductors. *Rev. Sci. Instrum.* **71**, 176–181 (1999).
40. H. Mori, N. Sakurai, S. Tanaka, H. Moriyama, T. Mori, H. Kobayashi, A. Kobayashi, Control of electronic state by dihedral angle in θ-type bis(ethylenedithio)tetraselenafulvalene salts. *Chem. Mater.* **12**, 2984–2987 (2000).
41. D. Vollhardt, Dynamical mean-field theory for correlated electrons. *Ann. Phys.* **524**, 1–19 (2012).
42. A. Pustogow, M. Bories, A. Löhle, R. Rösslhuber, E. Zhukova, B. Gorshunov, S. Tomić, J. A. Schlueter, R. Hübner, T. Hiramatsu, Y. Yoshida, G. Saito, R. Kato, T.-H. Lee, V. Dobrosavljević, S. Fratini, M. Dressel, Quantum spin liquids unveil the genuine Mott state. *Nat. Mater.* **17**, 773–777 (2018).
43. M. Dressel, A. Pustogow, Electrodynamics of quantum spin liquids. *J. Phys. Condens. Matter* **30**, 203001 (2018).

44. T. Sato, K. Miyagawa, K. Kanoda, Electronic crystal growth. *Science* **357**, 1378–1381 (2017).

45. K. Bender, I. Hennig, D. Schweitzer, K. Dietz, H. Endres, H. J. Keller, Synthesis, structure and physical properties of a two-dimensional organic metal, Di[bis(ethylenedithiolo) tetrathiofulvalene] triiodide, (BEDT-TTF)$^+_2$I$^-_3$. *Mol. Cryst. Liq. Cryst.* **108**, 359–371 (1984).

46. D. Schweitzer, P. Bele, H. Brunner, E. Gogu, U. Haeberlen, I. Hennig, I. Klutz, R. Świetlik, H. J. Keller, A stable superconducting state at 8 K and ambient pressure in α_t–(BEDT–TTF*)$_2$I$_3$^{1}. *Phys. B Condens. Matter* **67**, 489–495 (1987).

47. N. Ocelic, A. Huber, R. Hillenbrand, Pseudoheterodyne detection for background-free near-field spectroscopy. *Appl. Phys. Lett.* **89**, 101124 (2006).

48. A. L. Roytburd, Thermodynamics of polydomain heterostructures. I. Effect of macrostresses. *J. Appl. Phys.* **83**, 228–238 (1998).

49. L. D. Landau, E. M. Lifshitz, J. B. Sykes, W. H. Reid, E. H. Dill, Theory of elasticity: Vol. 7 of course of theoretical physics. *Phys. Today* **13**, 44–46 (1960).

50. J. D. Eshelby, The continuum theory of lattice defects, in *Solid State Physics Advance Research Applied*, F. Seitz, D. Turnbull, Eds. (Academic Press, 1956), vol. 3, pp. 79–144.

51. Y. F. Gao, W. Lu, Z. Suo, A mesophase transition in a binary monolayer on a solid surface. *Acta Mater.* **50**, 2297–2308 (2002).

52. S. M. Allen, J. W. Cahn, A microscopic theory for antiphase boundary motion and its application to antiphase domain coarsening. *Acta Metallurgica* **27**, 1085–1095 (1979).

53. J. Crank, P. Nicolson, A practical method for numerical evaluation of solutions of partial differential equations of the heat-conduction type. *Math. Proc. Cambridge Philos. Soc.* **43**, 50–67 (1947).

54. M. Alnæs, J. Blechta, J. Hake, A. Johansson, B. Kehlet, A. Logg, C. Richardson, J. Ring, M. E. Rognes, G. N. Wells, The FEniCS Project Version 1.5. *Arch. Numer. Softw.* **3**, 100 (2015).

55. A. Pustogow, "Unveiling Electronic Correlations in Layered Molecular Conductors by Optical Spectroscopy," thesis, University of Stuttgart (2017).

Citation: A. Pustogow, A. S. McLeod, Y. Saito, D. N. Basov, M. Dressel, Internal strain tunes electronic correlations on the nanoscale. *Sci. Adv.* **4**, eaau9123 (2018).

Science Advances

Internal strain tunes electronic correlations on the nanoscale

A. Pustogow, A. S. McLeod, Y. Saito, D. N. Basov and M. Dressel

ARTICLE TOOLS	http://advances.sciencemag.org/content/4/12/eaau9123
SUPPLEMENTARY MATERIALS	http://advances.sciencemag.org/content/suppl/2018/12/10/4.12.eaau9123.DC1
REFERENCES	This article cites 50 articles, 3 of which you can access for free http://advances.sciencemag.org/content/4/12/eaau9123#BIBL
PERMISSIONS	http://www.sciencemag.org/help/reprints-and-permissions